Nanoscale

PAPER

Cite this: *Nanoscale*, 2023, **15**, 13708

Polycrystalline bismuth nanowire networks for flexible longitudinal and transverse thermoelectrics

Luc Piraux, *[a] Nicolas Marchal, [a] Pascal Van Velthem, [a] Tristan da Câmara Santa Clara Gomes, [a] Etienne Ferain, [a,b] Jean-Paul Issi[a] and Vlad-Andrei Antohe *[a,c]

Received 10th July 2023,
Accepted 2nd August 2023

DOI: 10.1039/d3nr03332e

rsc.li/nanoscale

This paper reports on the preparation and the characterization of structural, electrical and thermoelectric properties of nanocomposite films formed from three-dimensional networks of polycrystalline bismuth (Bi) nanowires (NWs). The samples were fabricated by electrodeposition within polycarbonate (PC) templates with crossed cylindrical nanopores, yielding self-supported networks of Bi crossed nanowires (CNWs) with mean diameter values ranging from 23 nm to 230 nm. Temperature changes in electrical resistance and thermopower were studied by considering electric and thermal currents flowing in the plane of the films. While the values of the Seebeck coefficient are close to those of polycrystalline Bi for diameters greater than 100 nm, a progressive decrease in thermopower appears at smaller diameters, due to an increasing contribution of surface charge carriers as the diameter decreases. Transverse thermoelectricity based on the Nernst effect was also demonstrated on a network of Bi CNWs 230 nm in diameter. Such hierarchical architectures based on Bi CNWs are extremely robust, offering a reliable solution for the next generation of flexible thermoelectric devices.

1 Introduction

Bismuth (Bi) nanowires (NWs) have attracted much attention because of their predicted improved thermoelectric performances.[1–7] Indeed, in addition to the low Fermi energy values and effective charge carrier masses in Bi NWs, theoretical studies predict a transition from semi-metal to semiconductor below a critical diameter (≈50 nm depending on the crystal orientation) due to the quantum confinement effect.[2,8,9] Although the study of the dependence of thermoelectric power on the diameter of individual Bi NWs and parallel NW arrays has been the subject of several previous studies, the experimental results are very contrasted, not allowing the identification of a clear trend.[1,5,6,10–18] Several factors are likely to be at the origin of the puzzling results obtained on Bi NW arrays. Firstly, most measurements have been made on single crystal Bi NWs, some of which display different crystal orientations. Due to the strong anisotropy of the thermoelectric properties in bulk Bi, different results are therefore expected than those obtained on polycrystalline NWs obtained by electrodeposition (ECD). Secondly, thermal contact resistance is an important concern, and it is difficult to obtain a reliable estimate of the temperature gradient established in the out-of-plane direction of alumina or polymer membranes containing parallel NW arrays, due to the thinness of the porous templates and the large cross-sectional area/thickness ratio of the measured samples. In addition, the thermal contact resistances generally increase when the system is cooled, which makes their estimation very difficult.

The recent development of three-dimensional (3D) networks of interconnected NWs has opened up new prospects in the field of flexible thermoelectric materials.[19–23] These networks of crossed nanowires (CNWs), incorporated into 3D porous polymer membranes to form nanocomposite films, meet the essential requirements of electrical, thermal and mechanical stability. The temperature and diameter evolutions of the thermopower of electrodeposited Bi CNWs have been recently reported by applying out-of-plane thermal gradients.[24] Interestingly, unlike parallel arrays of NWs where thermal and electric current can only be applied in the direction parallel to the axis of the NWs, the 3D NW structure also allows measurements to be made in the macroscopic direction of the film plane, taking advantage of the excellent electrical connectivity.[19,21]

[a]*Institute of Condensed Matter and Nanosciences (IMCN), Université catholique de Louvain (UCLouvain), B-1348 Louvain-la-Neuve, Belgium.*
E-mail: luc.piraux@uclouvain.be
[b]*it4ip s.a., Avenue Jean-Etienne Lenoir 1, B-1348 Louvain-la-Neuve, Belgium*
[c]*R&D Center for Materials and Electronic & Optoelectronic Devices (MDEO), Faculty of Physics, University of Bucharest, 077125 Măgurele, Ilfov, Romania.*
E-mail: vlad.antohe@fizica.unibuc.ro

On the other hand, interest in the development of transverse energy conversion devices has recently received a boost due to the emergence of new classes of materials and new transport phenomena in transverse geometry.[25–28] Among the various transverse thermoelectric effects, the well-known Nernst effect generates a voltage transverse to the temperature gradient and the magnetic field. Therefore, semi-metals are of interest because they have mobile electrons and holes that deflect in opposite directions in a magnetic field so that their contributions add up, instead of partially compensating each other in longitudinal thermoelectric devices based on the Seebeck effect. For example, single-crystal Bi shows very high Nernst thermopower due to the very high mobility of charge carriers and the low Fermi energy.[26,29,30] Besides, since transverse devices do not require the use of separate n- and p-type materials, the thermoelectric module configuration using the Nernst effect is simpler than that using the Seebeck effect. In addition, as the Nernst voltage is generated in a direction perpendicular to that of the thermal gradient, its amplitude increases proportionally to the length of the sample along the direction of the electric field. This makes it possible to improve the performance of transverse thermoelectric devices by adjusting the dimensions and geometrical characteristics of a single material. Although an external magnetic field is required to exploit the Nernst effect, a magnetic field of 1 T can be easily obtained using a permanent neodymium magnet.

In this work, we report the fabrication and characterization of Bi CNWs obtained by ECD within flexible polymer membranes with crossed cylindrical nanopores. The evolution of structural and transport properties of Bi CNWs as a function of diameter, *i.e.*, between 23 nm and 230 nm, was studied by means of X-ray diffraction (XRD), temperature variation of electrical resistance and thermoelectric measurements. The measurements of the Seebeck coefficient as a function of temperature and for the different diameters were performed in a configuration where the thermal gradient is applied in the plane of the nanocomposite film. In addition, we first demonstrated the possibility of performing transverse thermoelectric measurements on CNWs, which is not possible for parallel NW arrays. A large Nernst signal was obtained at room temperature in a 230 nm diameter Bi CNW sample.

2 Materials and methods

2.1 Samples preparation

Analytical grade reagents (Merck) were used in this work as provided. Ultra-pure deionized water (DIW) supplied from a Milli-Q (Merck) system was employed for preparing the electrolytic solutions and for rinsing the samples during their fabrication process. A gaseous nitrogen (N_2) cylinder (5.0 purity from Praxair) was engaged in blow-drying operations.

Polycarbonate (PC) templates with a thickness of 28 μm have been first prepared by a track-etching method, following a well-established modified protocol.[19,31–35] Compared to the conventional track-etching technology, herewith the polymer films have been exposed to a sequential multi-step irradiation with heavy-ions under an angular range in respect to the normal of the PC surface prior to the chemical etching of the latent tracks in NaOH solution, hence allowing the formation of crossed cylindrical nanopores.[36] For present study, PC templates with different pore diameters (d) were prepared, *i.e.*, 23 nm, 28 nm, 45 nm, 105 nm and 230 nm.

Subsequently, a chromium/copper/chromium/gold (Cr/Cu/Cr/Au) multi-layered metallic electrode was e-beam evaporated *in situ* onto one side of the PC templates to act as cathode during Bi ECD. Apart of the ultra-thin Cr films (~15 nm) used as intermediate adhesion layers, the thickness of the Cu layer was regulated from ~2 μm for the PC template with 230 nm pores diameter to ~500 nm for the one with 23 nm diameter, while the thin top Au layer (~100 nm) was mainly deposited to prevent any Cu oxidation during the overall fabrication process flow. Noteworthy, the Cu layer thickness was carefully adjusted for the different PC templates to secure an uniform and consistent nanopores coverage withstanding Bi ECD process.

Bi ECD followed a slightly modified protocol as described elsewhere.[24,37,38] In brief, the electrochemical process was carried out in an aqueous electrolyte containing: 1 M HCl (hydrochloric acid fuming, 37%), 0.1 M $BiCl_3$ (bismuth chloride), 0.3 M $C_4H_6O_6$ (tartaric acid), 1 M NaCl (sodium chloride) and 1 M $C_3H_8O_3$ (glycerol). Bi was grown in the crossed nanopores of the PC templates *via* pulsed chronoamperometry, by applying to the working electrode (the metal-coated PC templates) a sequence of short voltage pulses *versus* a silver/silver chloride (Ag/AgCl) reference electrode (potassium chloride – KCl saturated, E = 0.197 V against normal hydrogen electrode – NHE) from a PAR 263A Potentiostat/Galvanostat, while a platinum (Pt) strip was immersed in the bath to act as the counter electrode. In this process, −0.35 V was applied for 10 ms as an electrochemical reduction step of Bi close to the working electrode' surface, and it was followed by −0.12 V for 90 ms as a relaxation period, providing time for the ions' concentration in the vicinity of the electrode to be replenished between consecutive reduction pulses. In this way, the multi-pulse electrodeposition process guaranteed a homogenous Bi filling of the crossed nanopores. The overall process duration was adjusted to obtain similar volumetric filling of the PC templates with different nanopore diameters.

The samples representing dense networks of interconnected Bi NWs embedded in the PC templates were afterwards thoroughly rinsed with DIW, subsequently dried-out under a soft stream of N_2 gas and then kept under normal environmental conditions until further manipulations.

2.2 Samples characterization

Morphological observations of the self-supported interconnected networks of Bi NWs were first performed using a JEOL 7600F field-emission scanning electron microscope (SEM). In this regard, the electrodeposited samples with cathode-side facing downwards were glued on a small silicon (Si) substrate using carbon tape, and subsequently only for SEM imaging purpose, the nanoporous PC template was thoroughly chemi-

cally removed by dropwise addition of dichloromethane for about 10 min.

Structural characterization of the Bi CNWs was afterwards performed by means of XRD using a Bruker D8 Advance diffractometer equipped with a Lynxeye XE-T detector, operating with Cu K_α radiation (λ = 0.15406 nm) at 1200 W (30 mA, 40 kV). XRD data were acquired at room temperature in a symmetric theta–theta (Bragg–Brentano) geometry, in the range of 2θ = 25°–75° with an angular step of 0.015° and an integration time of 0.15 s. The as-prepared samples were first subjected to an electrochemical etching procedure to completely remove the electrode layers from one side of the PC templates, and then carefully installed on a Si crystal sample holder. The cathode etching procedure was carried out galvanostatically in a commercially available Cu electrolyte, at a current density of 0.5 A cm^{-2}. EVA software package (Bruker) was used for data acquisition and post-processing, whilst ICDD (International Center of Diffraction Data) database was employed for phases identification. For displaying purposes, the amorphous background coming from the PC templates was extracted from the XRD patterns. Ultimately, the raw XRD data were subjected to a Rietveld refinement procedure using MAUD software,[39] in order to accurately compute the structural parameters of the Bi CNWs.

For conducting two-probe electrical and thermoelectric transport measurements, the cathode layers from one side of the PC templates were locally removed by electrochemical etching, as previously explained. In the two-probe configuration shown in Fig. 1a and b, the current is directly injected into the branched NW structure (about 1 cm long) from the unetched sections of the metallic cathode, where electrical contacts are made by silver paint.[19,40] The electrical and thermal current flows in the plane of the nanocomposite film following a zig-zag path along the segments of the Bi CNWs taking advantage of their high degree of electrical connectivity. Typical resistance values of the prepared specimens are in the range of few tens of ohms. For each sample, input power is kept below 0.1 μW to avoid self-heating. Temperature-dependent electrical resistance of Bi CNWs with 23 nm $\leq d \leq$ 230 nm was measured between 10 K and 320 K.

For the measurement of the Seebeck coefficient, heat flow in the plane of the CNW film is generated by a resistive heater anchored on a Cu block at one end of the sample, the other end being in good thermal contact with a heat sink. A thermoelectric voltage ΔV is generated by the temperature difference ΔT between the two metal electrodes, as shown in Fig. 1b. The voltage leads were made of thin chromel P wires, and the contribution of the leads to the measured thermoelectric power

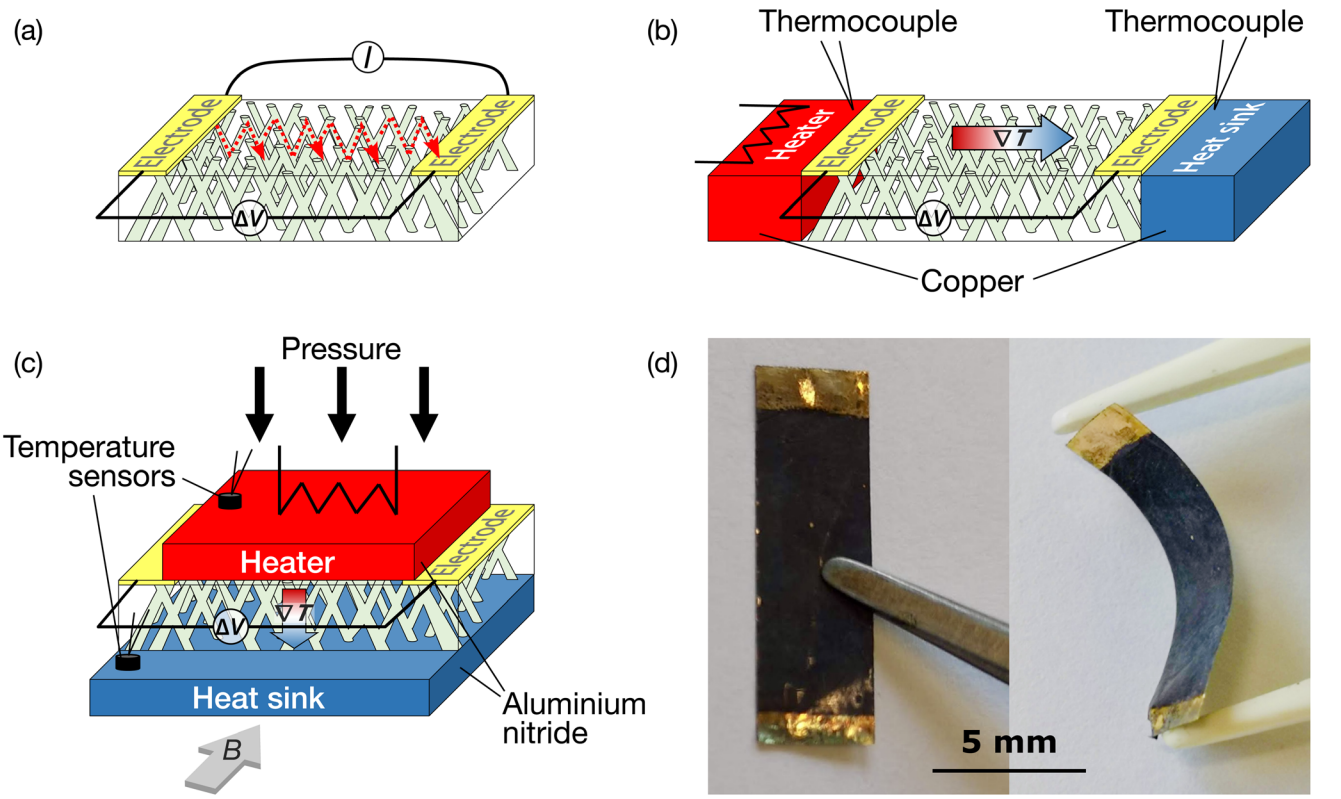

Fig. 1 (a and b) Two-probe electrode design obtained by local etching of the cathode layers for measurements of the electrical resistance and Seebeck coefficient of the 3D networks of crossed nanowires (CNWs). Heat flow in (b) is established in the plane of the Bi CNW film. (c) Design of the experimental set-up for transverse thermoelectric measurements where the heat flux is generated along the normal to the plane of the film. (d) Photographs of a flexible polycarbonate (PC)–Bi CNWs nanocomposite film after partial electrochemical etching of the cathode, showing metal electrodes at both ends for electrical and thermoelectric measurements. The photograph on the right side highlights the flexibility of the device.

was subtracted out using the recommended values for the absolute thermopower of chromel P in NIST ITS-90 Thermocouple Database. The temperature gradient was monitored with a small diameter type E differential thermocouple. A typical temperature difference of 1 K was used in the measurements. Seebeck measurements on Bi CNWs with 23 nm $\leq d \leq$ 230 nm were conducted between 100 K and 320 K under vacuum conditions.

Transverse thermoelectric measurements on Bi CNWs with d = 230 nm were carried out at room temperature under vacuum conditions in fields up to 1 T. The porous PC template 28 μm thick is completely filled with CNWs to form uniform nanocomposite film. The sample is placed between two aluminum nitride (AlN) wafers of high thermal conductivity (~100 W m^{-1} K^{-1} at T = 300 K). A resistive heater (100 Ω) bonded to the upper AlN wafer (20 × 5 × 0.6 mm^3) allows a thermal gradient to be established along the normal to the film, as shown in Fig. 1c. Under the hot AlN wafer, the electrode that served as the cathode for the CNWs growth was completely electrochemically etched (as previously explained), except for two very narrow side electrodes that allowed the transverse thermoelectric voltage to be measured using thin manganin wires. The temperature of the two AlN wafers are measured using calibrated Cernox™ sensors (mass ≤ 3.0 mg). To limit a major source of error when making transverse thermoelectric measurements on thin samples, it is also essential to minimise the thermal resistance of the contacts between the thermal conductors and the sample. In this regard, a very thin layer of Apiezon grease was used to improve the thermal contact between the nanocomposite film and the AlN wafers. Moreover, as recent work has shown,[41] mechanical pressure applied perpendicular to the sandwich is essential as well to significantly reduce the thermal resistance of the contacts. Here, the pressure is provided by a rigid rod with low thermal conductivity that firmly fixes the sample block shown in Fig. 1c. In addition, the thermal contact resistance must be determined to correctly estimate the temperature difference applied to the active material. As detailed below, the latter is estimated from a similar measurement carried out on a non-porous polycarbonate film of the same thickness and known thermal conductivity.

Photographs of a rectangular flexible sample representing Bi CNWs embedded in the PC template and with metallic electrodes at both ends, as-prepared for both electrical and thermoelectric measurements, are shown in Fig. 1d. The image on the right emphasizes the device' mechanical flexibility.

3 Results and discussion

3.1 Morphological and structural characterization

Fig. 2 shows SEM images of the obtained networks of Bi CNWs with various diameters, *i.e.*, 230 nm (Fig. 2a and b), 105 nm (Fig. 2c), 45 nm (Fig. 2d), 28 nm (Fig. 2e) and 23 nm (Fig. 2f), after the complete chemical dissolution of the PC membrane using dichloromethane. The homogeneity and self-supporting

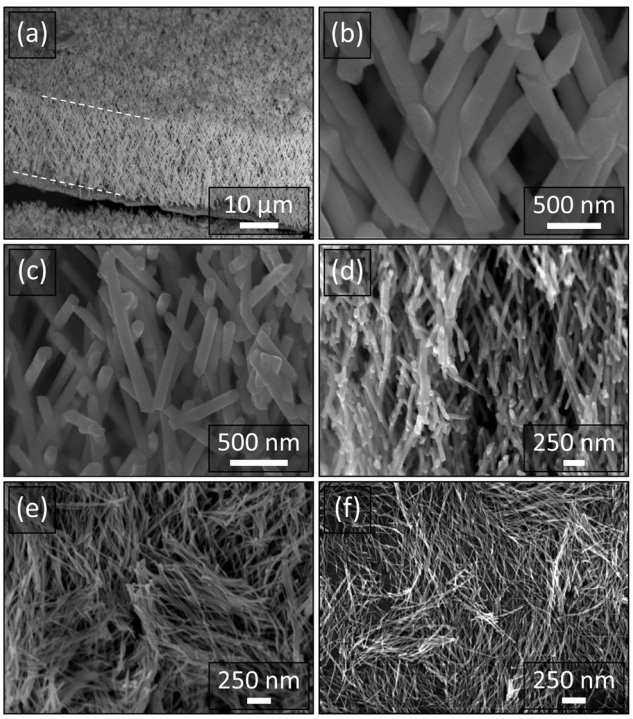

Fig. 2 (a) Low-magnification scanning electron microscope (SEM) image of the self-supported network of interconnected Bi CNWs with the diameter of 230 nm. Dashed markers indicate bottom (cathode side) and top network's borderlines, respectively. (b) Corresponding magnified image of the Bi CNWs branched structure. (c–f) High-magnification SEM micrographs of the interconnected networks of Bi CNWs with diameters of 105 nm (c), 45 nm (d), 28 nm (e) and 23 nm (f).

nature of the Bi CNWs with a diameter of 230 nm can be observed in the low-magnification image presented in Fig. 2a, where the dashed lines indicate the bottom- and top-side borders of the interconnected network. Also, the corresponding magnified image (Fig. 2b) suggests an uniform filling of the PC template, together with a high degree of NWs interconnectivity. It can be noticed as well that when reducing the nanopores diameter (Fig. 2c–f), the self-supporting structure of interconnected Bi CNWs perfectly replicates the 3D nanoporous PC templates, even for diameters as low as 23 nm (Fig. 2f). The uniform filling of the PC templates resulting in such complex branching structures is most likely attributed to the optimized multi-pulsed ECD process engaged in the samples preparation. However, following the complete removal of the nanoporous PC templates, the overall mechanical stability of the Bi CNWs gradually reduces with decreasing the NWs diameter, as also emphasized by the SEM micrographs.

Fig. 3 shows the XRD patterns of the samples containing Bi CNWs of different diameter values ranging from 230 nm to 23 nm. For convenience, the reference XRD pattern for Bi bulk powder, according to the ICDD 00-044-1246 card, is given in blue at the bottom of the graph. As can be noticed, the normalized XRD patterns include multiple peaks, demonstrating the polycrystalline nature of the Bi CNWs for all samples, with

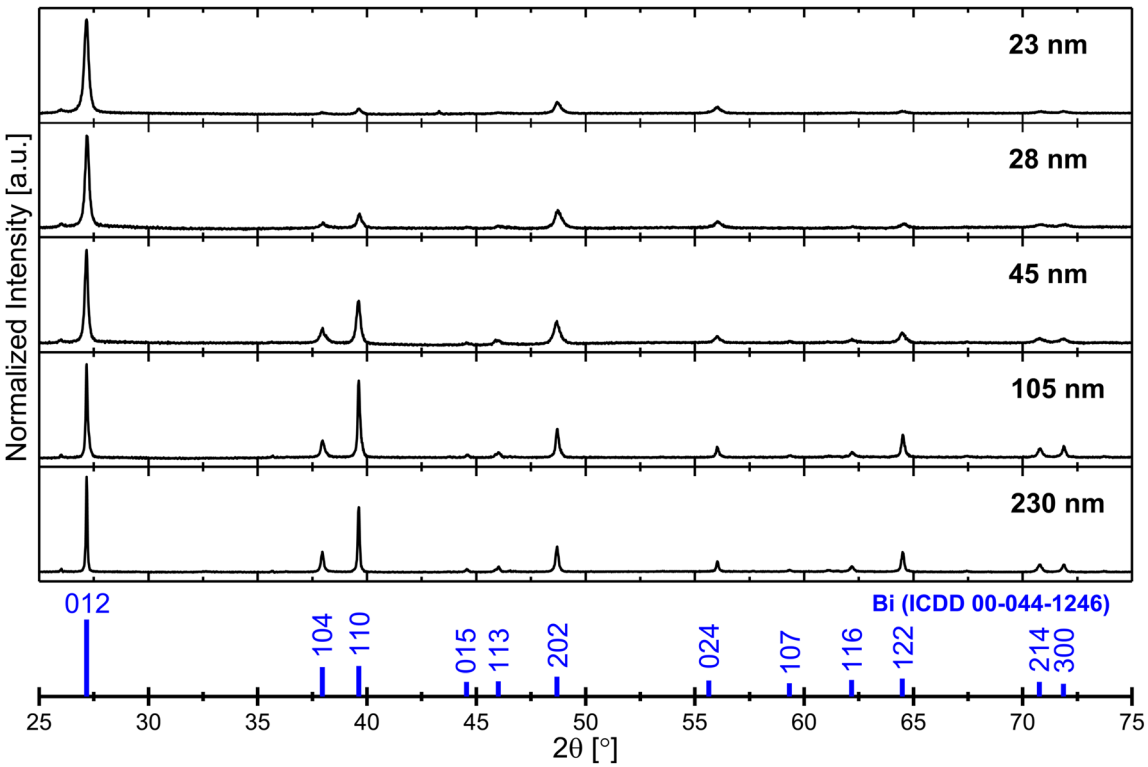

Fig. 3 X-ray diffraction (XRD) patterns acquired onto the Bi CNWs of average diameter values ranging from 23 nm to 230 nm, as electrodeposited within their corresponding PC template. The XRD patterns are normalized and shown after removing the amorphous background associated to the PC template. Reference powder diffraction data of Bi according to the ICDD 00-044-1246 card is shown in blue at the bottom.

the most intense peak shown at 27.16°, given by reflections from (012) planes of the Bi rhombohedral crystal structure. The overall observed weak preferential growth of the Bi CNWs can be obviously explained by the broad angular orientation of the Bi NWs electrodeposited within PC templates with crossed cylindrical nanopores, as opposed to other reports demonstrating a preferred growth orientation when developing vertically-aligned Bi NWs in anodic aluminium oxide templates (AAO).[37,42] However, a slight improvement of the texture with a preferential trigonal orientation along (012) plane can be observed with decreasing the diameter value towards 23 nm.

More importantly, it can be also seen that the shape of the peaks varies among the different samples, clearly indicating a change in the crystallite size of the Bi CNWs when lowering the mean diameter value from 230 nm down to 23 nm. In particular, the effect is more pronounced for the peaks reflected by the (012), (104), (110) and (202) planes, respectively, being suggested by their progressive broadening with decreasing the mean diameter value. This behavior could be related to a reduction in the crystalline coherence length (D_{ef}) with lowering the diameter of the Bi CNWs. Indeed, as shown in Table 1, the Rietveld refinement of the XRD patterns has proven a monotonous decrease of the crystallite size from (386 ± 11) nm for the Bi CNWs with diameters of 230 nm, to (58 ± 1) nm for the Bi CNWs with diameters of 23 nm. The obtained D_{ef} values suggest an elongated crystallite shape oriented along the NW

Table 1 Structural parameters of the Bi CNWs featuring different mean diameter values, as quantitatively obtained by Rietveld refinement of the XRD experimental data. D_{ef} denotes the crystalline coherence length (*i.e.*, crystallite size), $\langle\varepsilon^2\rangle^{1/2}$ is the mean square micro-strain, a and c represent the lattice parameters of the Bi rhombohedral crystal system (for Bi bulk powder, $a_{Bi_{bulk}}$ = 4.547 Å and $c_{Bi_{bulk}}$ = 11.862 Å, according to the ICDD 00-044-1246 card)

Diameter of the Bi NWs (nm)	D_{ef} (nm)	$\langle\varepsilon^2\rangle^{1/2}$	a (Å)	c (Å)
230	386 ± 11	$1 \times 10^{-3} \pm 2 \times 10^{-5}$	$4.546 \pm 5 \times 10^{-5}$	$11.857 \pm 4.1 \times 10^{-4}$
105	195 ± 4	$1.3 \times 10^{-3} \pm 4 \times 10^{-5}$	$4.545 \pm 7 \times 10^{-5}$	$11.853 \pm 6.1 \times 10^{-4}$
45	78 ± 1	$1.4 \times 10^{-3} \pm 8 \times 10^{-5}$	$4.545 \pm 1.2 \times 10^{-4}$	$11.846 \pm 9.8 \times 10^{-4}$
28	60 ± 1	$1.4 \times 10^{-3} \pm 1.5 \times 10^{-4}$	$4.542 \pm 2.5 \times 10^{-4}$	$11.858 \pm 1.71 \times 10^{-3}$
23	58 ± 1	$1.7 \times 10^{-3} \pm 5 \times 10^{-5}$	$4.541 \pm 2.2 \times 10^{-4}$	$11.853 \pm 1.54 \times 10^{-3}$

axis in the PC template. The latter remark could be sustained also by the values of the mean square micro-strain ($\langle\varepsilon^2\rangle^{1/2}$) exhibiting an overall increasing tendency with decreasing the Bi CNWs diameter, corroborated with a slight progressive reduction of the rhombohedral lattice parameter (a) in respect to the bulk value ($a_{Bi_{bulk}}$ = 4.547 Å), as the Rietveld refinement demonstrated (see Table 1).

4 Electrical and thermoelectric measurements

The temperature variation of the thermoelectric power (α) between 100 K and 320 K of the Bi CNWs with various diameters (23 nm ≤ d ≤ 230 nm) is shown in Fig. 4a. For the 230 nm diameter sample, both the temperature dependence and the measured values of α are close to those of polycrystalline bulk Bi and micro-sized Bi wires.[44–46] For the 105 nm diameter sample, the thermopower value at room temperature (RT) is identical to that of the 230 nm sample ($\alpha \sim -60$ μV K^{-1}) while the absolute values are slightly lower as the temperature decreases. In contrast, for smaller diameters, there is a significant reduction in negative thermopower, associated with a more pronounced linear temperature dependence indicating a dominant diffusion thermopower. It appears that the results of Fig. 4a differ from those recently reported through measurements along the normal direction of interconnected Bi NWs films with diameters between 40 nm and 140 nm.[24] Indeed, while a reduction in the magnitude of α with diameter reduction is also found (*i.e.*, see Fig. 5 in ref. 24), a sign change of the thermopower leading to positive values was observed at low temperature for diameters below 100 nm. On the contrary, no sign change of α is observed in the results of Fig. 4a, which also display significantly higher absolute α values. As pointed out above, the differences observed between our results and those of Wagner *et al.*[24] could be attributed to the two different measurement configurations used in the two studies. Indeed, while our measurements are carried out in the plane of the nanocomposite thin film, the out-of-plane measurements carried out by Wagner *et al.*[24] can lead to an overestimation of the temperature gradient across the thickness of the CNWs due to thermal contact resistances. In addition, previous theoretical and experimental studies on single crystal Bi NWs of various wire diameters have shown that the Seebeck coefficient changes sign from negative to positive at low temperature when measurement is performed along the bisectrix axis, while the thermopower remains negative along the binary and trigonal principal axes.[1,6,47] Therefore, no change in sign of the thermopower at low temperature is expected for polycrystalline electrodeposited Bi NWs. On the other hand, it is interesting to note that the reduction at room temperature of the thermopower of Bi CNWs when the diameter decreases is very similar to the evolution of the thermopower of polycrystalline Bi films obtained by electron-beam physical vapor deposition following a reduction in thickness,[43] as shown in Fig. 4b. These similar behaviors suggest that the same physical explanation can be considered to explain the reduction of the thermopower of polycrystalline Bi CNWs and films when the diameter or thickness is typically less than 100 nm. The diffusion thermopower of Bi includes the oppo-

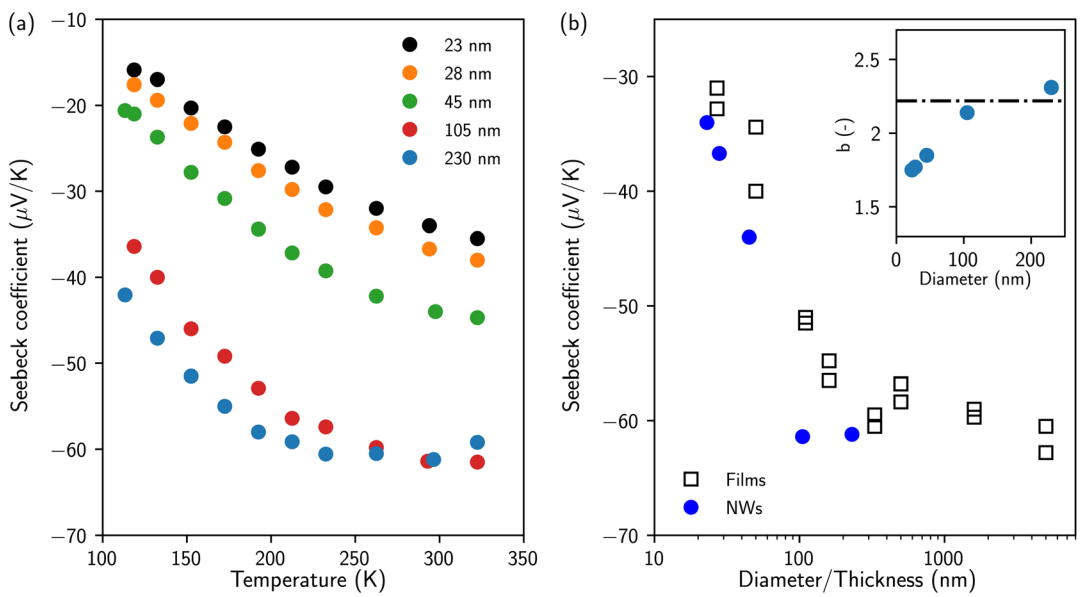

Fig. 4 (a) Temperature dependence of the Seebeck coefficient of interconnected Bi CNWs with various diameters. (b) Seebeck coefficient as a function of diameter of the Bi CNWs (blue circles); the data are compared to those obtained on polycrystalline Bi films (empty squares) of various thickness.[43] The inset shows the variation of the mobility ratio $b = \mu_n/\mu_p$ with NW diameter and the horizontal dashed line shows the minimum expected value of b when the mean free path of each carrier is limited by the NW diameter.

site sign contributions of electrons and holes. For a system with two types of charge carriers, the total thermopower α is expressed as follows:

$$\alpha = \frac{\alpha_n \sigma_n + \alpha_p \sigma_p}{\sigma_n + \sigma_p} \quad (1)$$

where α_n, α_p, σ_n, σ_p are the partial Seebeck coefficients and conductivities for electrons and holes, respectively. Assuming that the electron and hole carrier densities are identical, eqn (1) can be written as:

$$\alpha = \frac{\alpha_n b + \alpha_p}{b + 1} \quad (2)$$

where $b = \mu_n/\mu_p$ is the mobility ratio. According to previous studies and taking the approximate values for bulk Bi,[1,6,48] the partial Seebeck coefficients are expressed as:

$$\alpha_n = -\frac{\pi^2 k^2 T}{3e\gamma E_F^n} = -1.48 \times T\,\mu V\,K^{-2} \quad (3)$$

and

$$\alpha_p = +\frac{\pi^2 k^2 T}{3eE_F^p} = +2.23 \times T\,\mu V\,K^{-2} \quad (4)$$

where E_F^n = 27 meV and E_F^p = 11 meV are the Fermi energy for electrons and holes, respectively, while $\gamma = \left(1 + \frac{E_F^n}{E_g}\right) / \left(1 + \frac{2E_F^n}{E_g}\right) \sim 0.6$, with E_g = 13 meV the direct band gap energy at the L points of the Brillouin zone. Using the above expressions (3) and (4), it is possible to extract $b = \frac{\alpha_p - \alpha}{\alpha - \alpha_n}$ for each diameter from the linear variation of the thermopower measured in the low temperature range on the Bi CNW samples. The variation of the mobility ratio (b) with NW diameter is shown in the inset of Fig. 4b. We notice that the estimated value of b decreases with reducing the diameter. For the 230 nm sample, $b \sim 2.3$, which is close to that of micro-sized Bi wires, and smaller than that reported for polycrystalline bulk Bi ($b \sim 2.9$).[46] In a previous work, Murata *et al.*[13] proposed an approach based on the limitation of the mean free path to describe the evolution of the thermopower of Bi NWs as a function of diameter and temperature. This approach does not consider the semi-metal to semiconductor transition, as well as possible quantum effects and surface state conduction. In this model, it appears that the mobility ratio reaches a minimum value ($b \sim 2.22$) in the limit where the NW diameter determines the mean free path for both holes and electrons. As shown in the inset of Fig. 4b, values of $b < 2.22$ are obtained for $d < 100$ nm, with the deviation from this lower limit increasing as the diameter decreases. In addition, the α values for small diameter Bi NWs are lower than those predicted by the mean free path limitation model.[13] These indicate that other phenomena must be considered to explain the evolution of the thermopower with diameter.

Fig. 5 presents the temperature dependence of the normalized resistance to its value at room temperature for the Bi CNWs with 23 nm $\leq d \leq$ 230 nm. The temperature dependence of the electrical resistance of Bi CNWs is generally the result of the interplay of charge carrier density and mobility, which show contrasting variations with temperature.[6,10,13,46,47,49–52] For the 230 nm Bi CNW sample, the increase in resistance with decreasing temperature reflects the dominant contribution of the temperature change in carrier density, since their mobility weakly depends on temperature because of scattering processes dominated by NW surfaces and grain boundaries. On the contrary, the increase in resistance following a temperature decrease is much less pronounced for small diameter Bi NWs and a weak metallic behavior appears below $T \sim$ 100 K. It has been suggested that the quantum confinement leading to the semi-metal–semiconductor transition when the diameter is less than 50 nm is generally masked by the increasing importance of surface carriers as the diameter decreases.[5,7,53] Fig. 5 illustrates the increasingly important contribution of the metallic surface as the diameter decreases. The influence of diameter on the electrical resistance curves can also be compared to the thermopower results shown in Fig. 4. Indeed, while the transition from semi-metal to semiconductor should lead to an increase in thermopower for diameters less than 50 nm, the opposite behavior is observed. The absolute values of α decrease continuously as the diameter decreases due to the predominant contribution of the metallic surface.

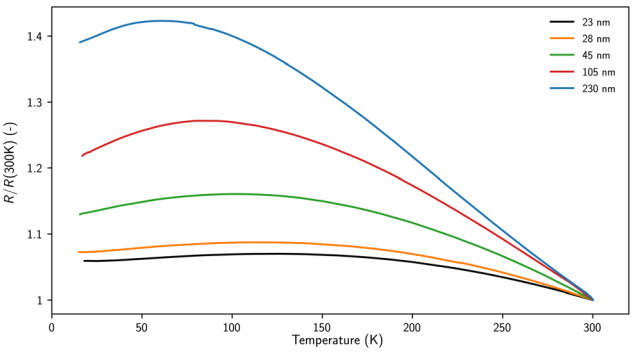

Fig. 5 Temperature dependence of the electrical resistance of Bi CNWs with various diameters. The data are normalized to values obtained at room temperature.

The results obtained at T = 300 K on a transverse thermoelectric device based on interconnected Bi CNWs (d = 230 nm) are reported in Fig. 6. In this measurement configuration, where the thermal gradient is applied perpendicular to the plane of the nanocomposite film, particular attention must be paid to the problem of thermal contact resistance. Indeed, this reduces the actual temperature difference across the Bi CNW film compared to the ΔT measured between the two AlN wafers using the Cernox™ sensors. The thermal contact resistance was estimated from calibration measurements performed on a non-porous PC film of the same thickness (28 μm) and cross-section (14.5 × 4 mm^2), of known thermal conductivity (0.2 W m^{-1} K^{-1}). The measured thermal conduc-

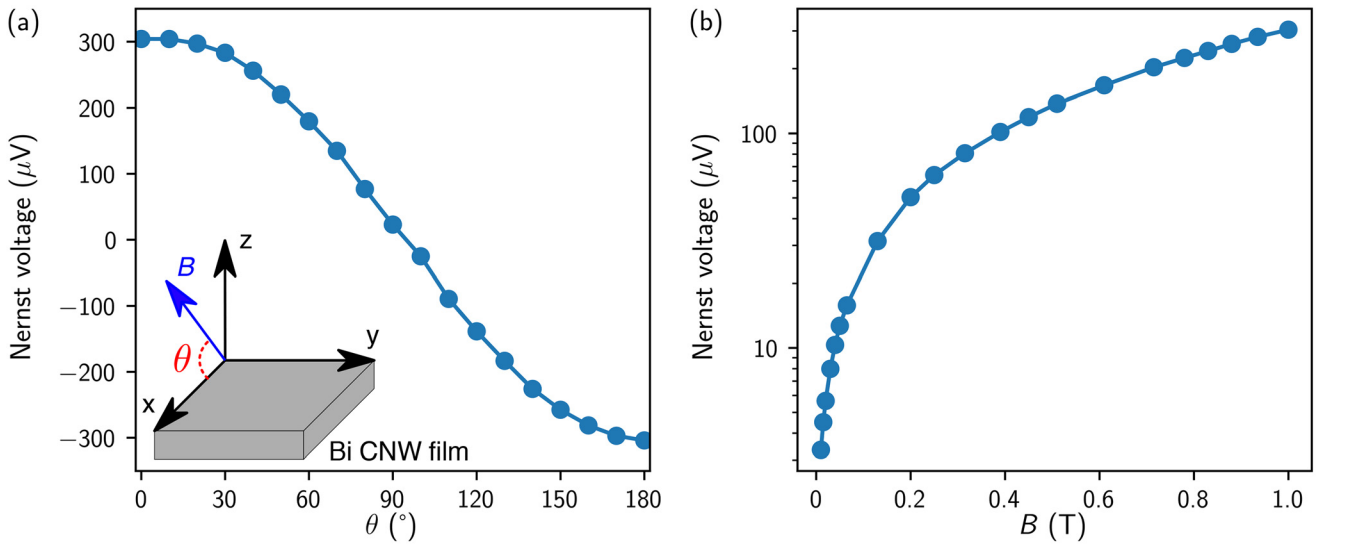

Fig. 6 (a) Room-temperature Nernst voltage at B = 1 T on 230 nm diameter Bi CNWs as a function of the angle between the magnetic field and the in-plane direction. The temperature difference across the Bi CNW film is 1 K. (b) Variation of the Nernst voltage as a function of the field intensity at T = 300 K when the magnetic field is applied perpendicular to the thermal gradient.

tance (0.37 W K^{-1}) was found to be slightly lower than the theoretical value (0.4 W K^{-1}) allowing us to estimate the thermal contact conductance (~4.6 W K^{-1}). Based on this calibration, the power dissipated in the heater was adjusted to ensure a temperature difference across the Bi CNW film of ΔT = 1 K with an uncertainty of 0.05 K. Fig. 6a shows the angular dependence of the transverse voltage on the temperature gradient for different orientations of a magnetic field of strength B = 1 T. When the field is applied along the normal to the nanocomposite film (which corresponds to the direction of the thermal gradient), the measured voltage is close to zero. On the contrary, in the measurement configuration where the in-plane magnetic field (B_x) is both perpendicular to the thermal gradient ($\nabla_z T$) and to the electric field (E_y), a high thermoelectric voltage, close to 300 μV, is obtained for ΔT = 1 K at an applied field strength of 1 T. The sinusoidal curve shown in Fig. 6a is a clear signature of the Nernst effect in 3D networks of Bi CNWs. The variation of the Nernst voltage with the strength of the magnetic field directed in the plane of the film is shown in Fig. 6b. The shape of the curve, which mainly follows a linear variation in field strength, is very similar to that obtained by performing transverse thermopower measurements on Bi single crystals.[26] As mentioned above, one of the advantages of transverse thermoelectric devices is that the performance can be increased by optimizing the extrinsic dimensions of the material. In particular, the output signal for a given value of the magnetic field can be considerably increased if the voltage measurement is made over a high distance compared to that over which the thermal gradient is imposed. This is precisely the case with our NW networks embedded within 3D porous membranes. Indeed, the thermal gradient is applied along the normal of a 28 μm thick film, while the Nernst voltage is measured between the electrical contacts 14.5 mm apart. Compared to the classical longitudinal thermoelectric geometry where the lengths associated with the ΔV and ΔT measurements are the same, the favorable geometry of our nanocomposite film leads to a factor $L_{\Delta V}/L_{\Delta T}$ ~ 518 increase in the Nernst signal:

$$S_{\mathrm{Nernst}} = E_y/\nabla_z T. \quad (5)$$

Furthermore, it should be added that the high thermoelectric voltages shown in Fig. 6a and b also result from the semimetallic character of Bi NWs. Indeed, pure Bi has an equal number of electrons and holes, which are deflected in opposite directions in a magnetic field, thus leading to additive contributions to the Nernst effect. Assuming that the effective surface area occupied by the Bi CNWs in the XY plane of the nanocomposite film is given by the product of the sample surface area and the membrane porosity (P ~ 10%) and because of the equivalent average linear density of the NWs along the X and Y directions, it is possible to estimate the Nernst signal measured along Y using the expression:

$$|S_{\mathrm{Nernst}}| \sim \left|\frac{\Delta V}{\Delta T}\right| \times \frac{L_{\Delta T}}{\sqrt{P} L_{\Delta V}}. \quad (6)$$

This leads to $|S_{\mathrm{Nernst}}|$ ~ 2 μV K^{-1} for B = 1 T. Although the Nernst signal in Bi CNWs is significantly lower than that measured in single crystal Bi at room temperature for the same field strength ($|S_{\mathrm{Nernst}}|$ ~ 30 μV K^{-1}) due to the low mobilities of the charge carriers in the NWs, it is comparable to that of other classes of materials potentially interesting for transverse thermoelectric devices.[26] In the low temperature range, the Nernst signal in single crystal Bi increases by several orders of magnitude, reaching record values (up to 30 mV K^{-1} at T = 6.8 K for a field strength of 1 T).[30] However, this huge increase in Nernst signal, linked to the very high mobilities of the free charge carriers (electron and holes) in single crystal Bi

at low temperature, is not expected in NW systems where surface scattering dominates.

5 Conclusions

In this work, we report on the fabrication, as well as on the structural and thermoelectric properties of 3D networks of polycrystalline Bi CNWs with mean diameter values ranging from 23 nm to 230 nm. The interconnected Bi CNWs were grown by ECD within 3D porous PC polymer membranes. The XRD results demonstrate the polycrystalline nature of the electrodeposited Bi CNWs, with a progressive XRD peak broadening with decreasing diameter, indicating a reduction in the crystalline coherence length. The temperature dependence of the electrical resistance and Seebeck coefficient were measured with an electrical and thermal current in the plane of the nanocomposite film following zig-zag paths along the segments of the interconnected Bi NWs. The thermopower of the 230 nm diameter sample shows the same negative values and temperature dependence as polycrystalline Bi with a maximum in the $\alpha(T)$ curve around room temperature and a value of -60 μV K^{-1}. A progressive decrease in thermopower appears for diameters smaller than 100 nm, due to the increasing importance of electronic surface states. For the 23 nm diameter sample, $\alpha \sim -33$ μV K^{-1} at $T = 300$ K. The predominant contribution of the metallic surface in small-diameter Bi CNWs is also corroborated by measurements of electrical resistance as a function of temperature. Taking advantage of the excellent electrical connectivity of the NW network, transverse thermoelectric measurements were also successfully performed on 230 nm diameter Bi CNWs. Since the length over which the Nernst voltage occurs in our experiment is more than a factor of 500 greater than the thickness of the NW-based film (28 μm) to which the thermal gradient is applied, large Nernst voltages were demonstrated at room temperature, reaching 300 μV at $B = 1$ T for $\Delta T = 1$ K. The estimated Nernst signal, $|S_{\mathrm{Nernst}}| \sim 2$ μV K^{-1} for $B = 1$ T is significantly lower than that measured in single crystal Bi at room temperature for the same field strength (~30 μV K^{-1}) due to the low mobilities of the charge carriers in the CNWs. As recently shown with magnetic NWs,[19–23] the template-assisted synthesis of 3D networks of interconnected NWs provides a simple and cost-effective pathway to fabricate flexible thermoelectric films with no sample size limitations and excellent control over geometrical features, morphology and chemical composition. These unique nanoarchitectures based on CNWS show great potential as lightweight, flexible and shapeable thermoelectric devices.

Author contributions

Luc Piraux: conceptualization, formal analysis, funding acquisition, investigation, methodology, project administration, resources, supervision, validation, visualization, writing – original draft, writing – review & editing; Nicolas Marchal: data curation, formal analysis, investigation, visualization; Pascal Van Velthem: formal analysis, investigation, methodology; Tristan da Câmara Santa Clara Gomes: data curation, formal analysis, investigation, visualization; Etienne Ferain: investigation, resources, visualization; Jean-Paul Issi: formal analysis, investigation, visualization, writing – review & editing; Vlad-Andrei Antohe: data curation, formal analysis, investigation, methodology validation, visualization, writing – original draft, writing – review & editing. All authors have read and agreed to the published version of the manuscript.

Conflicts of interest

There are no conflicts to declare.

Acknowledgements

Financial support was provided by Wallonia/Brussels Community (ARC 18/23-093) and the Belgian Fund for Scientific Research (FNRS). Authors would like to thank Flavio Abreu Araujo for his help in making the electrodeposited Bi CNW samples and François Devred for his help with the XRD measurements. J.-P. I. would like to thank Jean-Paul Minet and Benoit Hackens for growing and characterizing the Bi films (data presented in Fig. 4b). V.-A. A. would like to thank Claudiu Locovei for the discussions about the analysis of the XRD patterns.

References

1 J. Heremans and C. M. Thrush, *Phys. Rev. B: Condens. Matter Mater. Phys.*, 1999, **59**, 12579–12583.
2 Y. M. Lin, X. Sun and M. S. Dresselhaus, *Phys. Rev. B: Condens. Matter Mater. Phys.*, 2000, **62**, 4610–4623.
3 J. P. Heremans, C. M. Thrush, D. T. Morelli and M. C. Wu, *Phys. Rev. Lett.*, 2002, **88**, 216801.
4 J. P. Heremans, in *Thermoelectric Materials 2003: Volume 793: Research and Applications*, ed. T. P. Hogan, D. C. Johnson, G. S. Nolas and J. Yang, Materials Research Society, 1st edn, 2004, pp. 3–14.
5 T. E. Huber, A. Adeyeye, A. Nikolaeva, L. Konopko, R. C. Johnson and M. J. Graf, *Phys. Rev. B: Condens. Matter Mater. Phys.*, 2011, **83**, 235414.
6 A. Nikolaeva, T. E. Huber, D. Gitsu and L. Konopko, *Phys. Rev. B: Condens. Matter Mater. Phys.*, 2008, **77**, 035422.
7 J. Kim, W. Shim and W. Lee, *J. Mater. Chem. C*, 2015, **3**, 11999–12013.
8 L. D. Hicks, T. C. Harman and M. S. Dresselhaus, *Appl. Phys. Lett.*, 1993, **63**, 3230–3232.
9 X. Sun, Z. Zhang and M. S. Dresselhaus, *Appl. Phys. Lett.*, 1999, **74**, 4005–4007.

10 Z. Zhang, X. Sun, M. S. Dresselhaus, J. Y. Ying and J. Heremans, *Phys. Rev. B: Condens. Matter Mater. Phys.*, 2000, **61**, 4850–4861.
11 Y. M. Lin, O. Rabin, S. B. Cronin, J. Y. Ying and M. S. Dresselhaus, *Appl. Phys. Lett.*, 2002, **81**, 2403–2405.
12 Y. Hasegawa, D. Murata, D. Nakamura, T. Komine, T. Taguchi and S. Nakamura, *J. Electron. Mater.*, 2009, **38**, 944–949.
13 M. Murata, D. Nakamura, Y. Hasegawa, T. Komine, T. Taguchi, S. Nakamura, C. M. Jaworski, V. Jovovic and J. P. Heremans, *J. Appl. Phys.*, 2009, **105**, 113706.
14 D. Nakamura, M. Murata, Y. Hasegawa, T. Komine, D. Uematsu, S. Nakamura and T. Taguchi, *J. Electron. Mater.*, 2010, **39**, 1960–1965.
15 D. Nakamura, M. Murata, H. Yamamoto, Y. Hasegawa and T. Komine, *J. Appl. Phys.*, 2011, **110**, 053702.
16 J. Kim, S. Lee, Y. M. Brovman, P. Kim and W. Lee, *Nanoscale*, 2015, **7**, 5053–5059.
17 J. Kim, J. W. Roh, H. Moon and W. Lee, *J. Appl. Phys.*, 2017, **122**, 034303.
18 M. F. P. Wagner, A. S. Paulus, W. Sigle, J. Brötz, C. Trautmann, K. O. Voss, F. Völklein and M. E. Toimil-Molares, *Sci. Rep.*, 2023, **13**, 8290.
19 T. da Câmara Santa Clara Gomes, F. A. Araujo and L. Piraux, *Sci. Adv.*, 2019, **5**, eaav2782.
20 F. A. Araujo, T. da Câmara Santa Clara Gomes and L. Piraux, *Adv. Electron. Mater.*, 2019, **5**, 1800819.
21 T. da Câmara Santa Clara Gomes, N. Marchal, F. A. Araujo and L. Piraux, *Nanomaterials*, 2020, **10**, 2092.
22 L. Piraux, *Appl. Sci.*, 2020, **10**, 1832.
23 T. da Câmara Santa Clara Gomes, N. Marchal, F. A. Araujo and L. Piraux, *Nanomaterials*, 2023, **13**, 1735.
24 M. F. P. Wagner, A. S. Paulus, J. Brötz, W. Sigle, C. Trautmann, K. O. Voss, F. Völklein and M. E. Toimil-Molares, *Adv. Electron. Mater.*, 2021, **7**, 2001069.
25 A. Sakai, S. Minami, T. Koretsune, T. Chen, T. Higo, Y. Wang, T. Nomoto, M. Hirayama, S. Miwa, D. Nishio-Hamane, F. Ishii, R. Arita and S. Nakatsuji, *Nature*, 2020, **581**, 53–57.
26 S. R. Boona, H. Jin and S. Watzman, *J. Appl. Phys.*, 2021, **130**, 171101.
27 M. Murata, K. Nagase, K. Aoyama, A. Yamamoto and Y. Sakuraba, *iScience*, 2021, **24**, 101967.
28 Y. Pan, B. He, T. Helm, D. Chen, W. Schnelle and C. Felser, *Nat. Commun.*, 2022, **13**, 3909.
29 T. C. Harman and J. M. Honig, *Adv. Energy Convers.*, 1963, **3**, 525–528.
30 J. H. Mangez, J. P. Issi and J. Heremans, *Phys. Rev. B: Solid State*, 1976, **14**, 4381–4385.
31 E. Araujo, A. Encinas, Y. Velázquez-Galván, J. M. Martínez-Huerta, G. Hamoir, E. Ferain and L. Piraux, *Nanoscale*, 2015, **7**, 1485–1490.
32 L. Piraux, V. A. Antohe, E. Ferain and D. Lahem, *RSC Adv.*, 2016, **6**, 21808–21813.
33 A. Vlad, V. A. Antohe, J. M. Martínez-Huerta, E. Ferain, J. F. Gohy and L. Piraux, *J. Mater. Chem. A*, 2016, **4**, 1603–1607.
34 J. O. Omale, P. V. Velthem, V. A. Antohe, A. Vlad and L. Piraux, *Energy Technology*, 2021, **9**, 2100062.
35 J. O. Omale, R. Rupp, P. V. Velthem, V. V. Kerckhoven, V. A. Antohe, A. Vlad and L. Piraux, *Energy Storage Mater.*, 2019, **21**, 77–84.
36 E. Ferain and R. Legras, *Nucl. Instrum. Methods Phys. Res., Sect. B*, 2003, **208**, 115–122.
37 L. Li, Y. Zhang, G. Li and L. Zhang, *Chem. Phys. Lett.*, 2003, **378**, 244–249.
38 L. Li, Y. Zhang, G. H. Li, W. H. Song and L. D. Zhang, *Appl. Phys. A*, 2005, **80**, 1053–1055.
39 L. Lutterotti, *Nucl. Instrum. Methods Phys. Res., Sect. B*, 2010, **268**, 334–340.
40 T. da Câmara Santa Clara Gomes, J. D. L. T. Medina, Y. G. Velázquez-Galván, J. M. Martínez-Huerta, A. Encinas and L. Piraux, *J. Appl. Phys.*, 2016, **120**, 043904.
41 A. Sola, V. Basso, M. Kuepferling, M. Pasquale, D. C. né Meier, G. Reiss, T. Kuschel, T. Kikkawa, K. i. Uchida, E. Saitoh, H. Jin, S. J. Watzman, S. Boona, J. Heremans, M. B. Jungfleisch, W. Zhang, J. E. Pearson, A. Hoffmann and H. W. Schumacher, *IEEE Trans. Instrum. Meas.*, 2019, **68**, 1765–1773.
42 S. J. Limmer, W. G. Yelton, K. J. Erickson, D. L. Medlin and M. P. Siegal, *Nano Lett.*, 2014, **14**, 1927–1931.
43 J.-P. Issi, *et al.*, unpublished data.
44 T. Arisaka, M. Otsuka, M. Tokitani and Y. Hasegawa, *J. Appl. Phys.*, 2019, **126**, 085101.
45 J.-P. Issi, in *Thermoelectrics Handbook: Macro to Nano*, ed. D. M. Rowe, CRC Press, Taylor & Francis Group, *6000 Broken Sound Parkway NW, Suite 300*, Boca Raton, FL 33487-2742, 1st edn, 2006, *ch*. 30, pp. 1–12.
46 Y. Hasegawa, M. Murata, D. Nakamura, T. Komine, T. Taguchi and S. Nakamura, *J. Appl. Phys.*, 2009, **105**, 103715.
47 M. Murata, A. Yamamoto, Y. Hasegawa, T. Komine and A. Endo, *J. Appl. Phys.*, 2017, **121**, 014303.
48 J. Heremans and O. P. Hansen, *J. Phys. C: Solid State Phys.*, 1979, **12**, 3483.
49 R. Hartman, *Phys. Rev.*, 1969, **181**, 1070–1086.
50 J. P. Issi, *Aust. J. Phys.*, 1979, **32**, 585–628.
51 O. P. Hansen and I. F. I. Mikhail, *Phys. Status Solidi B*, 1984, **126**, 721–728.
52 J. Heremans, C. M. Thrush, Y. M. Lin, S. Cronin, Z. Zhang, M. S. Dresselhaus and J. F. Mansfield, *Phys. Rev. B: Condens. Matter Mater. Phys.*, 2000, **61**, 2921–2930.
53 P. Hofmann, *Prog. Surf. Sci.*, 2006, **81**, 191–245.